Paleoproterozoic melt-depleted lithospheric mantle in the Khanka block, far eastern Russia: Inferences for mobile belts bordering the North China and Siberian cratons

Dmitri Ionov, Guo Peng, Wendy R. Nelson, Steven B. Shirey, Matthias Willbold

Paleoproterozoic melt-depleted lithospheric mantle in the Khanka block, far eastern Russia: inferences for mobile belts bordering the North China and Siberian cratons

Dmitri A. Ionov[a*], Peng Guo[a, b], Wendy R. Nelson[c,d], Steven B. Shirey[d], Matthias Willbold[e]

[a] *Géosciences Montpellier, Université de Montpellier, 34095 Montpellier, France*

[b] *College of Earth Sciences, Jilin University, Changchun 130061, China*

[c] *Department of Physics, Astronomy and Geosciences, Towson University, Towson, MD 51252, USA*

[d] *Department of Terrestrial Magnetism, Carnegie Institution for Science, Washington, DC 20015-1305, USA*

[e] *Abteilung Isotopengeologie, Georg-August-Universität Göttingen, Göttingen 37077, Germany*

Corresponding author: dionov@umontpellier.fr (D.A. Ionov)

ABSTRACT *(309 words)*

The eastern part of Asia between the North China and Siberian cratons contains orogenic belts formed by the Paleo-Asian and Pacific subduction and older continental blocks. A fundamental question regarding these and all mobile belts is the fate of the continental lithospheric mantle (CLM) during their formation, i.e. whether, or to what extent the CLM may be formed, replaced or affected during orogeny. Insights into these processes can be obtained from mantle xenoliths hosted by Cenozoic basalts in the Proterozoic Khanka block in the far eastern Russia between NE China and the Pacific coast of Asia. We report petrographic, chemical, and Os-Sr-Nd isotope data for spinel peridotite xenoliths at two Khanka sites: Sviyagin and Podgelban. The modal abundances and chemical compositions suggest that the peridotites are residues of low to moderate degrees of melt extraction from fertile mantle. They show an $^{187}Os/^{188}Os$ vs. $^{187}Re/^{188}Os$ correlation with an apparent 1.9 Ga age; the $^{187}Os/^{188}Os$ ratios are positively correlated with Al_2O_3 and other melt extraction indices. These results provide the first robust CLM age constraints for the eastern Central Asian Orogenic Belt (CAOB). The ages suggest that the ancient CLM of the Khanka block may be roughly coeval with reworked CLM at Hannuoba (North China craton), and that it persisted through the Phanerozoic orogenies. Moreover, despite the proximity to Phanerozoic subduction zones, the Khanka CLM shows little post-melting enrichment, e.g. the clinopyroxenes are typically LREE-depleted and have Sr-Nd isotope ratios typical of the MORB mantle. We posit that the metasomatism of the CLM, earlier proposed for North China xenolith suites and ascribed to the effects of Pacific or older subduction and related mantle upwelling, may not be widespread in the CAOB. In general, Proterozoic blocks composed of residual peridotites may be more common in the CLM of the SE Siberia and northern China, and possibly other orogenic belts, than previously thought.

Keywords: mantle xenolith; peridotite; lithospheric mantle; partial melting; Re-Os isotope; Sr-Nd isotope; metasomatism

7495 words, 2 tables, 9 figures, 69 references; 3 electronic supplements

1. Introduction

The formation and evolution of the continental lithospheric mantle (CLM), which forms the lower portion of continental plates, is fundamental in the development of Earth's continents. Mantle xenoliths carried to the surface by volcanic eruptions are direct samples of the CLM that may provide valuable insights into its age, composition, structure as well as crust-mantle relations (e.g. Pearson et al., 2014; Rudnick and Walker, 2009; Walker, 2016).

The eastern part of the Asian continent comprises diverse, mainly Phanerozoic, terrains between the North China and Siberian cratons (Fig. 1). Most of these terrains make up the eastern segment of the Central Asian Orogenic Belt (CAOB) built up by collision and accretion of continental blocks and island arcs during northward subduction and closure of the Paleo-Asian Ocean in the Neoproterozoic to Early Mesozoic (e.g. Wilde, 2015). The CAOB is separated from the Asian Pacific margin by the Meso-Cenozoic Sikhote-Alin accretionary orogenic belt in far eastern Russia, related to the westward subduction of the Paleo-Pacific plate (e.g. Zhao et al., 2017).

The knowledge of age, composition and structure of the CLM is essential to better understand the multi-stage continental buildup and evolution of eastern Asia, as well as to evaluate the effects of the Paleo-Asian and Pacific subduction on the continental lithosphere. Geophysical and geochemical evidence suggests that the Archean lithospheric mantle of the North China craton was replaced by juvenile mantle at least twice: at around 1.9 Ga in response to collision events in the central craton, then in the Late Mesozoic in its eastern part (Gao et al., 2002; Liu et al., 2011; Menzies et al., 1993), most likely in relation to westward subduction of the Pacific slab (e.g. Liu et al., 2019; Xu, 2014; Zhu et al., 2012). Reworking and replacement affected the mantle lithosphere also beneath the central and southeastern (SE) Siberian craton (Ionov et al., 2005; Ionov et al., 2006a; Ionov et al., 2015).

By comparison, the age and composition of the CLM between the North China and Siberian cratons remain poorly constrained, especially due to the paucity of data on the mantle in the far eastern Russia between the northeastern (NE) China and the Pacific coast of Asia. While Cenozoic basaltic rocks hosting mantle xenoliths are widespread in far eastern Russia (Ionov et al., 1995; Nishio et al., 2004) and NE China (Xu et al., 1998; Xu et al., 1996) (Fig. 1), few CLM age estimates were reported for these localities. The estimates

that do exist encompass a broad range from Proterozoic to recent and are uncertain because they are based not on isochron dating methods, but on model Re-depletion (Guo et al., 2017; Wu et al., 2003; Zhang et al., 2011, 2019), Sm-Nd and Lu-Hf (Yu et al., 2009) age estimates for individual xenoliths, and are often controversial. Some recent papers invoke replacement of ancient CLM by juvenile materials and/or its extensive reworking often linked to Phanerozic subduction and recycled oceanic materials (Xu et al., 1996; Zou et al., 2014). However, the nature, distribution and formation processes for the inferred ancient, juvenile and metasomatic CLM components in this vast region remain poorly constrained.

Particularly rare are comprehensive data on mantle xenoliths from far eastern Russia. Ionov et al. (1995) reported petrographic and chemical data for eleven peridotite xenoliths from four sites in Sikhote-Alin. Ionov et al. (1999) and Kalfoun et al. (2002) described a few metasomatized xenoliths from northern Sikhote-Alin; Nishio et al. (2004) reported Sr-Nd and Li-isotope data for another five xenoliths. Finally, Guo et al. (2017) provided petro-geochemical and Re-Os isotope data for eight small xenoliths from the Khanka block.

In this study, we report on over 30 new, large and fresh peridotite xenoliths from two sites in southern far eastern Russia including petrography, major and trace elements in bulk-rocks and minerals, Sr-Nd isotope compositions for clinopyroxene (cpx), and Os isotope and siderophile element abundances for twelve whole rock peridotites.

This work allows us to describe comprehensively the CLM in the Khanka block and constrain its evolution. First, it consists mainly of residual peridotites with rare metasomatic overprints despite the proximity to Phanerozoic subduction zones. Second, the first robust age estimate based on $^{187}Os/^{188}Os$ vs. $^{187}Re/^{188}Os$ linear correlation is provided for the CLM in far eastern Russia and adjacent NE China. These results are significant also because the crystalline basement does not outcrop in the area and, therefore, it is not possible to constrain its age directly from a crustal section.

2. Geological setting and samples

2.1 Geological background

The continental domain in NE China and southern Siberia between the North China and Siberian cratons (Fig. 1) formed during two major tectonic events: (a) north-south closure of

the Neoproterozoic to early Mesozoic Central Asian and the Late Mesozoic Mongol-Okhotsk orogenic belts; (b) westward push related to the Pacific plate subduction that created the Sikhote-Alin Meso-Cenozoic accretionary orogenic belt in far eastern Russia; this geodynamic regime has dominated the regional tectonics since that time (e.g. Liu et al., 2017a). The eastern part of the CAOB in NE China is commonly referred to as the Xing'an-Mongolian Orogenic Belt (e.g. Xu et al., 2015) and is subdivided into several blocks (massifs); the Khanka block is the easternmost part of the CAOB that straddles the border with Russia (Fig. 1). All these blocks contain Precambrian rocks and/or detrital zircons and thus may include ancient continental fragments trapped in the CAOB (Zhou et al., 2018).

Cenozoic alkali basalts are widespread both in NE China and in the Russian Primorye (Maritime) region that includes the Sikhote-Alin Mountains and plains near the border with China (Fig. 1). Their origin is linked to continental extension and mantle convection induced by the subduction of the Paleo-Pacific plate (e.g. Okamura et al., 2005).

2.2 Xenolith localities and samples

Mantle xenoliths (Table 1) were collected at two sites in the Khanka block (Fig. 1): Sviyagin (44°80'N, 133°07'E) and Podgelban (43°62'N, 133°05'E). The first site is near the town of Sviyagino east of Lake Khanka, between the Trans-Siberian railway and the Ussuri (A-370) highway. Xenoliths reported in the literature (Guo et al., 2017; Ionov et al., 1995; Wang et al., 2015) are from alkali basalts at the junction of the highway with the road to Sviyagino (Plate 1, Electronic Supplement 1 (ES1)). The basalts may be linked to a nearby ~12 Ma old (Wang et al., 2015) volcanic center composed of tuffs and lava flows containing small (≤5 cm) xenoliths; bulk xenolith 8701-4 from this site reported by Ionov et al. (1995) was reanalyzed in this study. In contrast, all new samples in this study are from a basalt quarry south of Sviyagino (ES1) that exposed a ≥10 m thick lava flow or pool, which has the largest (10-15 cm) and least altered xenoliths in the area.

The Podgelban site is named after a stream in the Arsenievka River basin that crosscuts the NE part of the 9–12 Ma (Okamura et al., 1998) basalts of the Shkotov plateau, SE of Lake Khanka and north of the port of Nakhodka (Fig. 1). The samples are irregular

fragments in alkali basalts ~10 cm in size exposed along the stream.

Twenty-four Sviyagin and five Podgelban xenoliths were sawed to remove the rinds and thin-sectioned. Twenty of the largest (>100 g) and least altered peridotite samples, as well as a host Sviyagin basalt, were crushed by hammer in plastic sheets and their aliquots ground to powder in agate for whole rock (WR) analyses. Mineral grains were mounted in polished epoxy blocks for in-situ analyses. Essential petrologic and chemical information on the samples is listed in Table 1.

3. Methods

Major and minor element compositions of 20 WR samples were determined by wavelength-dispersive X-ray fluorescence (XRF) spectrometry at the Johannes-Gutenberg University, Mainz. The rock powders were ignited for ≥3 h at 1000°C, and the loss on ignition (LOI) calculated. Glass beads, produced by fusing 0.8 g of ignited powders with 4.8 g of dried LiB_4O_7 were analyzed on a Philips PW 1404 spectrometer using ultramafic and mafic reference samples as external standards. Peridotite reference samples JP-1 and UBN were analyzed as unknowns with results close to recommended values (Table 1, ES3).

Mineral major element compositions were determined by electron probe microanalysis (EPMA) at Montpellier University (MU) on a Cameca SX-100 using 15kV voltage, 15 nA current, counting times of 20–60 s for peaks and background and the 'X-PHI' quantification procedure. The modal abundances of the minerals in the rocks were calculated from a least-squares fit of the composition of the WR to its constituent minerals. The totals of the values obtained in the calculations are within ± 0.5% of 100%; they are reported normalized to 100%. Equilibration temperatures were calculated using cpx-opx thermometry (ES2).

The trace element concentrations of cpx were determined by laser ablation (LA) inductively coupled mass spectrometry (ICPMS) at the Max-Planck-Institute (MPI) for Chemistry in Mainz in grain mounts using a New Wave UP 213 Nd:YAG laser coupled to a ThermoFinnigan ELEMENT2 sector field. The beam size was 70 µm for cpx and up to 130 µm for opx. Trace elements in WR samples were measured by LA-ICPMS on fused glass beads at the MPI for Chemistry. About 130 mg of WR powder and ~10 mg of ultra-pure SiO_2 powder were homogenized to lower the melting temperature of the peridotites. About

40 mg of this mixture were molten on an iridium strip heater under Ar atmosphere at ~1550° C, then quenched by switching off the power and a simultaneous blast of cool Ar gas directed onto the lower side of the iridium strip.

Handpicked cpx (16–21 mg) from seven samples were acid-leached, dissolved and processed for separation of Sr and Nd prior to isotope analyses on a Triton Thermo-Fisher thermal ionization mass spectrometer (TIMS) at the MPI for Chemistry together with NIST SRM 987 Sr and La Jolla Nd. Mass fractionations were corrected to $^{86}Sr/^{88}Sr = 0.1194$ and $^{146}Nd/^{144}Nd = 0.7219$. Total procedure blanks are estimated as 46 pg for Sr and 14 pg for Nd.

Os isotope compositions and abundances of Re and platinum group elements (PGE) in twelve WR samples were determined at the Department of Terrestrial Magnetism, Carnegie Institution for Science (DTM-CIS). Powder aliquots of ~1.0 g were dissolved at 240°C in a reverse (2:1 HNO_3:HCl) aqua regia solution in Carius tubes (Shirey and Walker, 1995) with ~0.5 g of ^{185}Re-^{190}Os spike and ~1.5 g of a mixed ^{104}Ru-^{110}Pd-^{191}Ir-^{198}Pt spike. Osmium was removed from the aqua regia solution by a solvent extraction procedure (Cohen and Waters, 1996) using CCl_4 and then back-extracted using 9N HBr. Os was loaded from the HBr solution onto Pt filaments and followed when dry with a BaOH activator. Isotopic composition was measured on a Triton TIMS via peak hopping at typical signal sizes of 100–400 KCps for ^{192}Os and 3–15 KCps for ^{187}Os, and corrected to $^{192}Os/^{188}Os = 3.083$. $^{185}ReO_3^-$ was monitored for interference corrections, which were negligible for all samples. The average value measured for the DTM standard in the same period was $^{187}Os/^{188}Os = 0.17394 \pm 0.00008$. Four Os procedural blanks were measured: three of the blanks were <1 pg and one was <2 pg, which is negligible (~10^3 times lower than in samples in this study). Re, Ru, Ir, Pt, and Pd separates were analyzed using a Nu Plasma high-resolution multi-collector ICPMS. Four procedural blanks for the highly siderophile element (HSE) are as follows: Ir < 1 pg, Ru < 12 pg, Pt < 10 pg, Pd < 5 pg, and Re < 4 pg. Blank corrections are 2.5-8.6% of the measured abundance for Re, but negligible (< 1%) for Ir, Ru, Pt, and Pd.

A detailed description of all analytical procedures employed in this study is provided in the ES2. A complete set of analytical data for the samples and reference materials is given in ES3 (Tables 1-6).

4. Results

4.1 Petrography and modal compositions

Modal and WR major oxide compositions were obtained for 17 Sviyagin and three Podgelban xenoliths. All the samples are spinel lherzolites (Table 1). Sv-32 has the lowest cpx (6%) and highest olivine (72%), and is close in modal composition to a harzburgite (Fig. 2). The modal ranges in the other 19 samples analyzed in bulk are: 9–17% cpx, 51–66% olivine, 17–30% orthopyroxene (opx), and 1.0–2.5% spinel. The modal ranges for eight Sviyagin peridotites reported by Guo et al. (2017) are close to those in this study but show more scatter for cpx (Fig. 2), possibly because the modal estimates have more uncertainty due to small size of these samples. No discrete pyroxenite xenoliths or composite peridotites with pyroxenite or other veins have been found.

Photomicrographs of six representative Sviyagin xenoliths are given in Plate 2 of ES1. The rocks are medium-grained with texturally equilibrated mineral grains, protogranular, rarely porphyroblastic microstructures, and no strong fabric. The xenoliths show no evidence for invasion of host magma. A few of them have intergrowths of spinel and pyroxenes, cpx with spongy rims or, rare, tiny, fine-grained patches near spinel and cpx that contain silicate glass, feldspar, and Fe-Ti oxides. The xenoliths have no phlogopite or amphibole; olivine-rich Sv-32 has fine-grained apatite that contains 0.9% SrO, 3.6% Cl and 0.7% F (Ionov et al., 2006b). No sulfides have been found in the xenoliths in this study by optical inspection of polished thin sections in reflected light at normal to medium magnification.

Equilibration temperatures (T) for the Sviyagin samples (Table 1) define a broad range from 810 to 1000°C. This contrasts with significantly higher T's (993–1054°C) for the Podgelban xenoliths, which appear to come from a hotter (hence probably deeper) CLM section, although the T ranges at both localities overlap at ~1000°C.

4.2 Chemical composition of whole-rocks and minerals

The WR major element data for 20 peridotites in this study are given in ES3 (Table 1). They have low loss on ignition (LOI, -0.48 to 0.43 wt.%), consistent with low or negligible alteration from petrographic observations. Positive LOI values in the majority of the samples

mean that mass gain due to oxidation of FeO to Fe_2O_3 is greater than the loss of volatiles. Oxide co-variation plots with Al_2O_3 (a melt extraction index) are shown in Fig. 3 and Plate 3 of ES1. Al_2O_3 is negatively correlated with MgO and NiO concentrations and Mg# (molar Mg/(Mg+Fe)), is positively correlated with CaO, Na_2O, TiO_2 and to a lesser degree SiO_2 concentrations, and is not correlated with Cr_2O_3. High K_2O (0.03–0.11 wt.%) in six WR samples may be linked to minor amounts of interstitial silicate glass, microcrystalline feldspar and spongy cpx rims (Plate 2 of ES1).

None of the xenoliths have very fertile compositions overlapping primitive mantle (PM) estimates, unlike for peridotite suites from Tariat and Vitim (Carlson and Ionov, 2019; Ionov, 2002) in the central CAOB; however, some appear only mildly depleted (Fig. 3). The three Podgelban peridotites have higher modal cpx (Fig. 4d) and concentrations of Al_2O_3, CaO, Na_2O and TiO_2 than most Sviyagin xenoliths in this study (Fig. 3), though the number of the samples is too small for conclusive inferences on rock type proportions and compositions at the two sites. They are distinct in composition from five refractory peridotites (8803-1 to 8803-5) mistakenly reported by Ionov et al. (1995) as Podgelban samples because of labeling error.

An enigmatic feature of the Sviyagin xenolith suite is the unusually high concentrations of P_2O_5 (0.04–0.15 wt.%) in eleven WR peridotites. They cannot be due to contamination by host magma because of insufficiently high P_2O_5 (0.88 wt.%; ES3) in the host basalt, and the absence of correlations with Na, Al and other elements enriched in the basalt. Sample Sv-32 has the highest P_2O_5 and contains accessory apatite (Plate 2e, ES1; Ionov et al., 2006b) but, based on petrographic data, its modal abundance cannot be as high as 0.4% estimated from P_2O_5 in the WR (0.15 wt.%) and in the apatite (43 wt.%). In addition to optical microscopy, phosphates in five P_2O_5-rich (≥0.08%) xenoliths were sought using EPMA element mapping in stage scanning mode registering signals for P and BSE images (Ionov et al., 2006b). The mapping found microcrystalline phosphates forming crosscutting and interstitial veins and pockets suggesting they are secondary. They are similar to apatite in major oxide proportions, but distinct from mantle phosphates by very low totals (<90%) and low concentrations of Na, Cl and La (≤0.02%), yet have high F (1.8%) and SrO (1.9%) (Ionov et al., 2006b).

Major element compositions of minerals in 23 Sviyagin and five Podgelban peridotites

are given in Table 2 of ES3. Mg# of olivine ($Mg\#_{Ol}$), the major mineral host of Mg and Fe in whole rocks, shows a uniformly close-fitting correlation with the $Mg\#_{WR}$ (Fig. 4a), demonstrating high accuracy and reproducibility of the data obtained by different methods. The Cr# (molar Cr/(Cr+Al)) of spinel is positively correlated with $Mg\#_{Ol}$ (Fig. 4b) and negatively correlated with WR Al_2O_3 (Fig. 4c) and TiO_2 in cpx. Altogether, the major element variations are consistent with melt extraction trends (e.g. Carlson and Ionov, 2019; Herzberg, 2004; Pearson et al., 2014).

The major element ranges for eight Sviyagin peridotites reported by Guo et al. (2017) are similar to those in our collection. Most of the samples from the previous work plot with moderately fertile peridotites in this study and, in some cases, deviate slightly from the trends defined by our samples (Figs. 2–4). The WR differences may be related to smaller size and greater alteration of the samples in the earlier work.

4.3 Trace element composition of whole-rocks and minerals

Trace element compositions for 20 WR samples, cpx from 24 samples and opx from 14 samples are given in Tables 3 and 4 of ES3. The WR concentrations of Yb (Fig. 3f) and other heavy rare earth elements (HREE) correlate positively with Al_2O_3 indicating a coherent behavior of moderately incompatible major and trace elements usually attributed to the loss of a melt (McDonough and Sun, 1995). In contrast, the concentrations of trace elements more incompatible than medium REE (MREE) show broad variations usually unrelated to those of less incompatible elements; when normalized to primitive mantle (PM) they define complex patterns with common positive U and Sr abundance anomalies (Fig. 5a,b).

The cpx show parallel and similar patterns of more or less strong depletions in the light REE (LREE) relative to the MREE and the HREE (Fig. 5c); the only exception is sample Sv-17, in which both the cpx and the WR are LREE-enriched. Many cpx show slight enrichment of the MREE over the HREE caused by the greater partitioning of the HREE into opx, which is more obvious in samples with high modal opx/cpx ratios (e.g., Sv-32; see opx data below). Extended primitive mantle-normalized trace element patterns for cpx (Fig. 5d) show complex relations for highly incompatible elements with negative anomalies for

299 the high field strength elements (HFSE) Ti, Zr, Hf, Nb and Ta, strong positive anomalies for
300 U, and positive or negative anomalies for Sr. Samples Sv-7 (LREE-depleted) and Sv-17
301 (LREE-enriched) were selected for pyroxene analyses across grains in thin section (18
302 analyses for cpx Sv-7) to check their homogeneity. No core-rim differences have been found
303 in the cpx and opx grains in these samples indicating that inter-mineral chemical
304 equilibration has accompanied textural equilibration.
305 Primitive mantle-normalized REE patterns for opx (Fig. 6a) are smooth with steeper
306 HREE-LREE slopes than for the cpx while extended PM-normalized trace element patterns
307 (Fig. 6b) show significant positive anomalies for the HFSE that match (much weaker)
308 negative anomalies of these elements in coexisting cpx. The opx/cpx elemental ratios (Fig.
309 6c,d) show narrow ranges suggesting that the pyroxenes are in chemical equilibrium with
310 one another and with the bulk rocks (except for the highly incompatible Th, U, Nb, Ta that
311 normally are very low in opx, but may show spurious values due to micro-inclusions and
312 analytical challenges at very low concentrations).
313
314 *4.4 Os-Sr-Nd isotope compositions, and PGE and Re concentrations*
315 The $^{87}Sr/^{86}Sr$ and $^{143}Nd/^{144}Nd$ ratios for cpx from seven xenoliths are given in Table 5 of
316 ES3. They plot in the depleted segment of the mantle array (Fig. 7) because they have lower
317 $^{87}Sr/^{86}Sr$ (0.7023–0.7041) and higher $^{143}Nd/^{144}Nd$ (0.5128–0.5133) than the PM (BSE). Five
318 cpx are close to the DMM end-member in the MORB field (as well as three Sviyagin cpx
319 reported by Nishio et al. (2004)); two cpx (Sv-7 and Sv-32) are in the OIB field because of
320 lower $^{143}Nd/^{144}Nd$ (0.51284–0.51288) and higher $^{87}Sr/^{86}Sr$ (0.7036–0.7041) than the former;
321 these two samples are close in isotopic composition to the host Sviyagin basalt.
322 HSE concentrations and Os isotope ratios for twelve WR samples in this study are given
323 in Table 2 and in Table 6 of ES3. The PGE+Re patterns (Fig. 8) are nearly parallel and show
324 continuous depletions from Ir to Pt, Pd and Re (excepting two samples with minor Re
325 enrichments); seven Sviyagin xenoliths reported by Guo et al. (2017) show similar patterns.
326 The Os concentrations range from 1.0 to 2.9 ppb; their mean (1.9±0.9 ppb, 2σ) is close
327 to those reported for off-craton peridotite xenolith suites erupted by alkali basalts worldwide
328 (e.g. Pearson et al., 2004). The Os concentrations and Os/Ir ratios in the Sviyagin suite are

low relative to PM (Becker et al., 2006), which is also seen in many off-craton peridotite xenolith suites (Luguet and Reisberg, 2016; Rudnick and Walker, 2009). The loss of Os has been attributed to processes ranging from metasomatism and melt percolation in the mantle to sulfide breakdown or alteration during and after the transport, yet the Os isotopic ratios typically can remain unmodified by any of these processes (e.g. Reisberg et al., 2005).

The samples in this study show a positive $^{187}Os/^{188}Os$ vs. $^{187}Re/^{188}Os$ linear correlation ($^{187}Os/^{188}Os = 0.032\times^{87}Re/^{188}Os + 0.1148$). The array of data corresponds to general age of 1.91 Ga (Fig. 9a). To assess the uncertainty of this age pairs of lines were drawn parallel to the correlation: (a) through the upper and lower samples most remote from the correlation line (crossing $^{187}Os/^{188}Os$ axis at ~0.118 and 0.112, Fig. 9a); (b) comprising ten out of twelve samples; the latter cross $^{187}Os/^{188}Os$ axis at ~0.1165 and 0.113 corresponding to an age range of 2.25 and 1.78 Ga. We prefer to evaluate the data this holistic way rather than to use an isochron regression program because isochron regression programs are best suited to better correlated data arrays with low MSWD values. Using such programs with data arrays that have some scatter (high MSWD values) forces unsupported choices of which analyses to leave out of the regressions and then produces regression errors that may little geologic meaning when applied to the regressed age.

We believe that this age estimate is generally robust because the Os isotopic variation can be explained by Re decay and the $^{187}Os/^{188}Os$ ratios also define very tight-fitted linear correlations with CaO ($r^2 = 0.96$), MgO ($r^2 = 0.91$), Mg# ($r^2 = 0.90$), Al_2O_3 ($r^2 = 0.86$) and modal cpx ($r^2 = 0.92$) (Fig. 9c-d). Therefore, essential chemical and modal indices of the extent of melt extraction also control the Re/Os ratios in the melting residues and the ingrowth of radiogenic Os with time. Combining our samples with six Sviyagin xenoliths reported by Guo et al. (2017) (excepting a sample with anomalously high $^{187}Re/^{188}Os$ of 0.77) yields grouped age of 1.8 Ga and $r^2 = 0.95$ for the overall $^{187}Os/^{188}Os$ correlation with CaO. These age estimates agree well with the average T_{MA} of 1.95 Ga for Sviyagin samples in this study if a single sample with an anomalously high T_{MA} is omitted from consideration as well as with the median T_{MA} of 2.1 Ga (Table 2).

5. Discussion

5.1 The role of melt extraction and metasomatism in the origin of the Khanka peridotites

The CLM is believed to form from the convecting upper mantle, usually following large-scale melt extraction events. The partial melting conditions can be assessed from modal and chemical compositions of residual peridotites in comparison with experimental data on melting of fertile mantle. Plots of Al_2O_3 vs. FeO (Fig. 3a) in melting residues may constrain both pressure (P) and melting degrees because Al_2O_3 is a robust melt extraction index while FeO concentrations are controlled by pressure (Herzberg, 2004). The majority of the Khanka peridotites experienced low to moderate (≤20%) batch melting whereas two samples experienced 25–28% melting. The FeO variations in the Khanka xenoliths (Fig. 3a) suggest melting in a broad P range, mainly ≤1 GPa to 3 GPa, and up to 4 GPa for three rocks. The equilibration temperatures (hence depth of origin) for the Khanka xenoliths (810–1054°C) range broadly, and do not correlate with Al_2O_3, other melting indices or FeO, suggesting no compositional stratification of the CLM under this region.

An alternative way to evaluate melting degrees is to model the WR abundances of moderately incompatible trace elements, e.g. HREE (Plate 5, ES3) that are sensitive to melt extraction and least affected by metasomatism, during melting of fertile mantle (PM) based on mineral-melt partition coefficients and modal compositions. The model used here (Ionov et al., 2017; Takazawa et al., 2000) yields melting degrees of ~15% for the most refractory xenolith Sv-32 and 1–10% for other Khanka samples. These are the lowest possible melting degrees because the model uses incremental fractional melting at 1% steps, which extracts incompatible elements more effectively than batch partial melting in experimental work that provided major oxide indices of melting degrees (Herzberg, 2004) (Fig. 3a).

The sum of compositional data on the Khanka peridotites in this study is remarkably consistent with an origin of these rocks by low to moderate degrees of melt extraction from fertile mantle, with no or only minor post-melting effects. This inference is supported by well-fitting correlations of modal and major oxide WR compositions, mineral compositions, a coherent behavior of moderately incompatible major and trace elements (Figs. 3-4) as well as similarities to xenolith suites with proven melt extraction origins like Tariat in Mongolia (central CAOB) (e.g. Carlson and Ionov, 2019).

An outstanding feature of the Khanka peridotites in this study is that the co-variation

plots for TiO_2 and Na_2O with Al_2O_3 (Fig. 3d-e) and MgO have convex downward shapes (in particular if forced through the PM composition). This is consistent with melting trends calculated from experimental data (Takazawa et al., 2000) and thus suggests little or no overprinting by silicate-melt metasomatism. In contrast, the trends observed in most other worldwide peridotite suites are linear or vague (Rudnick and Walker, 2009) and thus may signify late-stage melt entrapment or addition during or after melting events.

The signs of metasomatism in the Khanka suite are scarce. It is dominated by peridotites that show LREE-depleted pyroxene and bulk-rock compositions, and contain chemically equilibrated minerals (Figs. 5 and 6; Plate 4, ES1) further indicating no significant addition of metasomatic media after its formation by melt extraction. Only one xenolith has LREE-enriched cpx. Rare, fine-grained interstitial materials and glass accompanied by elevated K_2O and P_2O_5 and enrichments in La (Fig. 5a) in some WR samples may be linked to the entrapment and transport of the xenoliths by host magmas. On the other hand, some xenoliths show enrichments in U and Sr, elements that are highly incompatible and mobile in hydrous fluids, not only in the WR but also in the cpx. These enrichments may have been introduced to the Khanka CLM by low-volume fluids linked to subduction events, similar to peridotites from island arcs that usually show enrichments in U and Sr and high U/Th (e.g. Ionov, 2010).

5.2 The age of the CLM in the Khanka block from Re-Os isotope data

The Sviyagin peridotites display one of the best $^{187}Os/^{188}Os$ vs. $^{187}Re/^{188}Os$ correlations reported as yet for a suite of mantle xenoliths (e.g. Rudnick and Walker, 2009). We attribute this to the fact that these samples represent melting residues that have not been overprinted by metasomatism. They appear to preserve relatively pristine Re-Os isotope systematics, not disturbed significantly by Re mobility (Fig. 8) in the mantle after melting or during xenolith transport, and therefore carry accurate age information on the CLM formation.

Though no statistically significant (with the sum of least squares less than 1) Re–Os isochrons have been reported for any WR peridotite suites, the $^{187}Os/^{188}Os$ vs. $^{187}Re/^{188}Os$ correlations for a suite of peridotite xenoliths from Hannuoba in the mobile belt crosscutting the North China craton (Gao et al., 2002) have been inferred to define robust CLM

formation ages (Liu et al., 2011; Rudnick and Walker, 2009). The eleven Hannuoba samples reported by Gao et al. (2002) define nearly the same regression slope, hence apparent age, as the twelve Sviyagin samples in this study and show similar scatter on the co-variation diagram (Fig. 9a). Gao et al. (2012) argued that the Re-Os isotope systematics in at least one Hannuoba xenolith had been disturbed, discarded three more samples plotting higher above the correlation line and used a regression for seven samples forced through the present-day PM composition to obtain an age of 1.91±0.22 Ga. This value is identical to the Re-Os age obtained without discarding any of the twelve Sviyagin xenoliths in this study and using our preference of considering the data array *in toto*, as discussed above. Nonetheless, applying an approach of Gao et al. (2012), i.e. consecutively disregarding Sviyagin samples with highest deviations from $^{187}Os/^{188}Os$ vs. $^{187}Re/^{188}Os$ regression line, and forcing it through the PM, yields ages from 1.8 to 2.3 Ga, depending on the selection of samples omitted from the calculation. These age estimates are identical within the error margins, and consistent with that from "alumina-chron" in Fig. 9b using $^{187}Os/^{188}Os$ value at 0.7 wt.% Al_2O_3 (e.g. Rudnick and Walker, 2009).

There are many reasons why statistically valid Re-Os isochrons cannot be obtained for mantle xenolith suites (e.g. Rudnick and Walker, 2009). Re-Os systematics in residual peridotites may be perturbed by metasomatism, inadequately sampled due to the nugget effect, modified during emplacement by contamination with relatively Re-rich host magmas, and weathered near the surface. These factors, however, may be comparatively less significant for the Sviyagin suite that shows no or little evidence for metasomatism (REE patterns) or alteration (low LOI's). More important may be the random way that mantle samples are picked up at depth. The xenoliths in this study come from a broad enough depth range that they were too far apart to equilibrate with each other during melting or be formed from a homogeneous source in a single melting episode. Rather, they likely formed in a series of roughly coeval or successive episodes of melting of heterogeneous asthenosphere. Overall, our data suggest that the CLM of the Khanka block formed in a Paleoproterozoic tectonothermal event, but do not allow us to constrain its timing or duration more precisely than the scatter on the Re-Os data array (Fig. 9a). But peridotite Re-Os age is important because despite the fact that the crystalline basement of the Khanka block is not exposed in

Russia, detrital zircons from the southern Sikhote-Alin in the vicinity of the Khanka block show a major ~1.8 Ga U-Pb age peak (e.g. Liu et al., 2017a), consistent with the Paleoproterozoic (~1.9 Ga) age for the Khanka CLM in this study.

5.3 Model age estimates of CLM formation

Earlier studies (Guo et al., 2017; Wu et al., 2003; Zhang et al., 2011, 2019) attempted to constrain the CLM formation age in NE China and the Khanka block using model Re-Os (T_{MA}) or Re-depletion (T_{RD}) estimates (Carlson, 2005; Walker et al., 1989) for individual xenoliths. Such an approach, however, is questionable for off-craton peridotites. The lack of ubiquitously high degrees of melt depletion, hence incomplete Re removal, usually means that Os T_{RD} ages do not reflect true melt depletion ages (Luguet and Reisberg, 2016; Pearson and Wittig, 2014). This is why these studies ascribe an ancient T_{RD} age obtained for a single sample, or a small number of most refractory samples, to the whole CLM domain, i.e. assuming that the oldest model age of a given suite could be used to define the age of melting. However, this can only be valid if the samples in the suite show a positive $^{187}Os/^{188}Os$ vs. $^{187}Re/^{188}Os$ correlation, i.e. evidence for the formation in a single event from a uniform source. By contrast, several lines of evidence suggest that the DMM, the presumed source of the CLM, has a range of Os isotopic compositions, including rocks or minerals with Proterozoic model ages (Rudnick and Walker, 2009; Walker, 2016), that may be older than true lithospheric formation ages of terrains in a given mobile belt (Carlson and Ionov, 2019). Similarly uncertain, for comparable reasons, are age constraints in the previous studies based exclusively on $^{187}Os/^{188}Os$ co-variation with melting indices (Reisberg and Lorand, 1995) for the peridotite suites.

Sr-Nd isotope compositions of cpx from seven out of ten Sviyagin xenoliths shown in Fig. 7 plot in the DMM field; many yield Proterozoic Rb-Sr (1.7–2.1 Ga) and Sm-Nd (1.0–1.6 Ga) model depletion ages relative to primitive mantle. Such estimates, however, are not likely to reflect melting events during CLM formation. Even the most fertile (4.0–4.5 wt.% Al_2O_3) unmetasomatized off-craton xenoliths, including those in the CAOB, may yield similar Sr-Nd isotope values (e.g. Ionov et al., 2005), which appear to be typical of shallow asthenosphere (e.g. Carlson and Ionov, 2019).

Wang et al. (2015) reported in situ Re-Os isotope data for interstitial sulfides in six Sviyagin xenoliths, with T_{MA} ranging from negative values to 3.7 Ga, and T_{RD} from 0.23 to 1.66 Ga (mainly 0.7–1.2 Ga), as well as two much older values (2.6 and 2.8 Ga). These values scatter broadly, may not be accurate, and likely record metasomatic rather than melting events. However, Wang et al. (2015) used them to infer a Mesoproterozoic CLM formation age, distinct from the Paleoproterozoic melting age obtained in this study.

We see at least three reasons why the WR Re-Os data in this study provide a better age estimate than those reported by Wang et al. (2015). (1) Whole-rock analyses can be obtained for any peridotites, not only those that contain sulfides, and therefore allow us to select the best and most representative samples from the xenolith suite. In contrast, large sulfides are required to obtain in-situ data on xenoliths. Therefore, samples analyzed by LA-ICPMS are, by definition, biased to the very few rocks that have a specific type of metasomatism, which introduces secondary sulfides. No large sulfides have been found in the xenoliths selected for this study by optical inspection of thin sections. (2) WR data represent a much larger volume of each xenolith, both in terms of the mass of the powder analyzed (1–2 g) and of xenolith material crushed (>100 g) and ground to powder (>20 g). Therefore, the WR data are based on a more representative sampling that includes large numbers of Os-hosting grains rather than the one advantageous grain that can be analyzed by LA-ICPMS. (3) Age estimates in this study are based on an array of $^{187}Os/^{188}Os$ vs. $^{187}Re/^{188}Os$ data for 18 xenoliths from two independent studies compared to model ages for individual sulfide grains from six xenoliths. This array also has an initial $^{187}Os/^{188}Os$ of ~0.116 that supports the formation of this block of CLM from the convecting mantle around 2 Ga.

Generally, the robustness, accuracy and relevance of the lithospheric formation age estimates from individual in-situ sulfide analyses by LA-ICPMS are doubtful, in particular for interstitial sulfides in off-craton peridotites (Pearson et al., 2014; Rudnick and Walker, 2009). The dominant Os hosts in pristine refractory peridotites are Os-Ir alloys. Sulfides are some of the first phases to enter the melt during melting even below the peridotite solidus, hence they are most likely metasomatic in nature in xenoliths (Lorand and Grégoire, 2006; Reisberg et al., 2005), in particular those sufficiently large for in situ analyses and, by definition, carry a mixed and uncertain Os isotope signal.

509

510 *5.4 Khanka peridotites compared with those in North China and CAOB*

511 It is relevant to compare mantle xenoliths from the Khanka block with those from the
512 adjacent North China in general and the eastern CAOB in particular. The Khanka peridotites
513 may have much in common with those from Hannuoba in the Trans-North China Orogen, at
514 the northern margin of the North China Craton (NCC) (Rudnick et al., 2004) where cratonic
515 CLM was replaced by juvenile material in the Paleoproterozoic. The Khanka and Hannuoba
516 peridotites have similar modal, major element, Os and Sr-Nd isotope ranges and age (Fig. 9).
517 On the other hand, the Hannuoba xenoliths show common LREE-enrichments, have
518 abundant, coarse sulfides and high S abundances as well as nearly flat, PM-like HSE
519 patterns (Gao et al., 2002; Liu et al., 2011). Little, if any, compositional distinction has been
520 found between the CLM of the NCC replaced in the Paleoproterozoic (Hannuoba) and in the
521 Phanerozoic (Qixia) (Rudnick et al., 2004).

522 Mantle xenoliths have been reported from several locations in NE China east and
523 southeast of the Khanka block: Shuangliao, Yitong, Jiaohe and Wangqing in the eastern
524 CAOB (Wu et al., 2003; Yu et al., 2009), Nuomin and Keluo in the Xingan block of the
525 CAOB as well as Huinan and Kuandian in the NE NCC (Fig. 1). In general, these sites have
526 more diverse xenolith types than in the Khanka block with harzburgites (Fig. 2), wehrlites
527 and pyroxenites being more common. The peridotites at each site in the eastern CAOB are
528 generally more refractory (averages: 1.9–2.4 wt.% Al_2O_3, 1.6–2.4 wt.% CaO, 40–43 wt.%
529 MgO) than in the Khanka block (Plate 3, ES1).

530 The majority of the Kelou xenoliths (Zhang et al., 2011) are metasomatized dunites,
531 harzburgites and low-cpx lherzolites. Zhang et al. (2011) interpreted a highly scattered
532 "alumino-chron" and ancient (~2 Ga) T_{RD} ages for three refractory rocks as representing
533 CLM formation ages decoupled from crustal ages. They also inferred unrealistically low
534 melt extraction degrees (3-11%) for the harzburgites owing to erroneous trace element
535 modeling. The nearby Nuomin xenolith suite (Zhang et al., 2019) is dominated by refractory
536 peridotites as well. Zhang et al. (2019) report a broad range of T_{RD} ages (0.5–1.6 Ga) for
537 these rocks, yet interpret them as fragments of coexisting Paleo-Mesoproterozoic and
538 Neoproterozoic CLM in the region, contrary to the evident fallacy of using single T_{RD}

estimates for individual off-craton xenoliths as CLM formation ages that represent a mantle portion (Rudnick and Walker, 2009; Walker, 2016). By comparison, xenoliths from Tariat in central Mongolia define an excellent "alumino-chron", but show no $^{187}Os/^{188}Os$ vs. $^{187}Re/^{188}Os$ correlation, which led Carlson and Ionov (2019) to interpret them as essentially undifferentiated MORB-source mantle that was accreted during the ocean-closing events that formed the CAOB.

The peridotites from Huinan (Xu et al., 2003) and Kuandian (Wu et al., 2006) in the NE NCC and some other sites have much higher FeO than experimental melting residues of fertile mantle (Plate 3, ES1; Herzberg, 2004), most likely due to reaction with Fe-enriched melts that may ultimately produce wehrlites (Ionov et al., 2005) or opx-rich peridotites (Xu et al., 2003), depending on melt compositions. As a result, the NE China peridotites tend to have higher FeO and lower Mg# and SiO_2 than the Khanka peridotites at similar Al_2O_3 (Plates 3–4, ES1), and also show a broader HREE range with mainly LREE-enriched REE patterns (Plate 6, ES1). This contrasts with the mainly LREE-depleted Khanka CLM.

Overall, the Khanka mantle xenoliths in this study are distinct in modal and chemical compositions from those in nearby localities in the eastern CAOB in NE China (Fig. 1). The Khanka CLM is dominated by moderately depleted lherzolites that are mostly unaffected by metasomatism and in this regard are more similar to xenolith suites in central Mongolia (Ionov, 2002, 2007; Carlson and Ionov, 2019) and southern Siberia (Ionov et al., 2005) to the west in the CAOB. This contrasts with higher proportions of harzburgites and other rocks (wehrlite, pyroxenite) overprinted by metasomatism, commonly attributed to subduction, in nearby NE China (eastern CAOB and the NE NCC) where the cratonic CLM was replaced or reworked in the Meso-Cenozoic.

5.5 The age and composition of CLM in orogenic belts

The CLM in orogenic belts may have a complex structure with a range of compositions and ages. One reason for this complexity is the varied nature of lithospheric components assembled in the belts, from island arcs and other oceanic domains with juvenile lithosphere to ancient continental fragments (micro-continents) (e.g. Zhou et al., 2018). The late Paleozoic to early Mesozoic subduction zones where the CAOB components were

assembled are located in central and southern Mongolia and NE China (e.g. Wilde, 2015) away from the North China Craton (NCC). Therefore, though southern CAOB borders on the NCC now, it was not built against or around it, and therefore is not likely to incorporate remobilized Archean CLM components.

Another reason for its complex structure is the potentially variable influence of subduction processes on these CLM domains during and after the closure of oceanic basins (e.g. Ionov et al., 2017; Liu et al., 2011). A fundamental question regarding the CLM in orogenic belts is whether it is expansively re-worked by the subduction-related metasomatism, or alternatively, the re-working is spatially limited.

The subduction of the Paleo-Asian and Pacific slabs has significantly influenced the lithospheric architecture of eastern China, including the destruction of the CLM in eastern NCC (Zhu et al., 2012), the formation of the Songliao basin in the easternmost CAOB (Liu et al., 2017b), and metasomatism in mantle xenoliths, either directly by slab-derived melts and fluids (Deng et al., 2017) or via related asthenospheric upwelling (Guo et al., 2017). Overall, literature data on basalt-hosted mantle xenoliths in NE China seems to suggest widespread and intense CLM re-working by metasomatism, though specific links between the subduction and CLM modification continue to be debated.

By comparison, the results in this study demonstrate for the first time that the CLM of the Khanka block, i.e. the nearest CAOB segment to the Asian Pacific margin, shows no or very limited metasomatic effects. Moreover, it retains chemical and isotopic signatures of its formation by melt extraction at ~2 Ga including Re-Os isotope relations. It follows that the CLM re-working in orogenic belts, both in the CAOB and worldwide, is not widespread and may be limited to weaker lithospheric portions that also concentrate basaltic magmatism. In this regard, the Khanka CLM resembles that in the Tariat region of central Mongolia in the central CAOB (Carlson and Ionov, 2019), which is composed mainly by very fertile lherzolites and thus is distinct from CLM typical of subduction zones (Arai et al., 2007; Ionov, 2010).

The factors determining the strength and stability of the CLM remain poorly constrained. The findings in this study suggest that relatively fertile, pyroxene-rich CLM domains may be more resistant to widespread metasomatic reworking, and ultimately to destruction, than

refractory, olivine-rich CLM. This may be related to better permeability of olivine-rich rocks to carbonatite as well as silicate metasomatic media (e.g. Ionov et al., 2006a).

The reason for the high proportion of metasomatized rocks among mantle xenoliths at some North China sites may be CLM reaction with source liquids of young mafic magmas that carry the xenoliths. If such sub-lithospheric liquids stall and fractionate in the lower CLM before the eruption, they will affect the host mantle. The situation may be similar to the high proportion (~60%) of sheared and metasomatized (Fe-Ti-rich) garnet peridotites among kimberlite-hosted xenoliths in the SE (Ionov et al., 2005, 2006a) and central Siberian craton (Agashev et al., 2013; Doucet et al., 2013). Chemical and geophysical modeling link the deformation and metasomatism in cratonic roots with kimberlite-related fluids, and demonstrate that the CLM with a high share of Fe-rich peridotites cannot be rheologically stable and long-living (Bascou et al., 2011; Doucet et al., 2014).

6. Summary of conclusions

The mantle xenoliths hosted by Cenozoic basalts in the Precambrian Khanka block in far eastern Russia between NE China and the Pacific coast of Asia, provide insights into the CLM of the eastern CAOB and other off-craton orogenic belts. The modal and chemical data suggest that the Khanka peridotites are residues of low to moderate degrees of melt extraction from fertile mantle with no or limited effects of metasomatism in spite of the proximity to subduction zones in the Pacific. This contrasts with the pervasive metasomatic reworking of the CLM beneath many adjacent regions, including NE China (e.g. Deng et al., 2017; Yu et al., 2009), SE Siberian craton (Ionov et al., 2006c) and the localities closer to the Pacific coast in far eastern Russia (Ionov et al., 1999; Ionov et al., 1995). The Sviyagin peridotites display one of the best $^{187}Os/^{188}Os$ vs. $^{187}Re/^{188}Os$ correlations reported for a mantle xenolith suite and provide the first robust CLM age constraint for the eastern CAOB. The Paleoproterozoic CLM of the Khanka block, with LREE-depleted cpx and Sr-Nd isotope ratios typical of the MORB mantle, persisted through Phanerozoic orogenies, unlike most of mantle xenoliths reported from nearby NE China. This study suggests that melt-depleted, but relatively fertile Proterozoic CLM domains in orogenic belts may not be expansively re-worked during the closure of ocean basins and collision events, and may be

tectonically resilient.

Acknowledgements

DAI thanks V. Prikhodko for guidance with fieldwork and acknowledges support from the Max-Planck-Institute (Mainz, Germany) in 2003-2005, and Chinese Academy of Sciences President's International Fellowship Initiative (PIFI) for Visiting Scientists in 2017 and in 2019 (Grant No. 2017VCA0009). PG acknowledges a fellowship from China Scholarship Council as a joint PhD student at the Montpellier University, France as well as financial support from the National Natural Science Foundation of China (Grant 91858211) and National Key Research and Development Project (2017YFC0601304).

Figure Captions

Fig. 1. A sketch map of NE China and southern far eastern Russia showing the tectonic framework, major areas of Cenozoic basaltic volcanism (grey fields) and mantle xenolith occurrences (stars). CAOB: Central Asian Orogenic Belt including its major tectonic units (blocks, massifs) in NE China: Erguna, Xing'an, Songnen, Jiamusi-Bureya and Khanka. The xenoliths in this study are from Sviyagin and Podgelban in the Khanka block.

Fig. 2. Modal compositions of peridotite xenoliths from the Khanka block in this study (filled circles) and those reported by Guo et al. (2017) (open circles) in comparison with peridotite xenoliths from the CAOB in NE China (Xu et al., 1998; Yu et al., 2009) as well as references on Chinese localities (grey squares) provided in ES1.

Fig. 3. Plots of Al_2O_3 vs. major oxide and Yb concentrations and Mg# (molar Mg/(Mg+Fe)) for whole-rock (WR) peridotite xenoliths from Khanka in this study (large filled circles) and those reported by Guo et al. (2017) (open circles). Also shown are primitive mantle (PM McDonough and Sun, 1995) and peridotite xenoliths from central CAOB (Tariat in Mongolia, small grey circles) that experienced melt extraction (Ionov, 2007; Ionov and Hofmann, 2007); the latter overlap the Khanka suite at moderate Al_2O_3 (melt depletion degrees) and extend the melting-related trends to the PM. Grey dashed lines are correlation trends (exponential trends show best fits for Na_2O and TiO_2), r^2 are correlation coefficients. Blue dotted lines in (a) show isobaric batch melting residues of fertile mantle at

1, 2, 3 and 4 GPa, continuous red lines are residues of polybaric fractional melting at 2–0, 3–0, 5–1 and 7–2 GPa (Herzberg, 2004). See online version for color code.

Fig. 4. Co-variation plots for Al_2O_3, Mg# (molar Mg/(Mg+Fe)) and modal cpx in WR xenoliths, Mg# in olivine and Cr# (molar Cr/(Cr+Al)) in spinel for xenoliths in this study and from Guo et al. (2017). Shown for comparison are peridotite xenoliths from central CAOB (Tariat in Mongolia, small grey circles) dominated by fertile spinel lherzolites (Ionov, 2007; Ionov and Hofmann, 2007). Exponential correlation trends (dashed grey lanes) show best fits for plots of $Cr\#_{spl}$, r^2 are correlation coefficients.

Fig. 5. Rare earth element (REE, left) and lithophile trace element (right) patterns for WR xenoliths (top) and clinopyroxenes (cpx, bottom) in this study normalized to primitive mantle (PM) (McDonough and Sun, 1995). The cpx patterns for all samples except Sv-17 show regular, continuous depletion from heavy and medium to light REE; cpx and WR Sv-17 is enriched in light REE. Xenolith Sv-32 has the lowest medium and heavy REE in the cpx (c) and WR (a) as well as the lowest modal cpx and Al_2O_3 (Fig. 4d). WR patterns (b) show common positive anomalies for U, Sr and Ba likely due to fluid metasomatism.

Fig. 6. PM-normalized (McDonough and Sun, 1995) REE (a) and lithophile trace element (b) patterns for orthopyroxene (opx), and the cpx/opx concentration ratios for the REE (c) and lithophile trace elements (d). The opx patterns in (a) show continuous, steep trends of depletion in less compatible REE. The cpx/opx show a coherent and narrow range for all but the most incompatible elements suggesting chemical equilibration of minerals in the rocks.

Fig. 7. Plots of $^{87}Sr/^{86}Sr$ vs. $^{143}Nd/^{144}Nd$ for clinopyroxene in xenoliths in this study (large circles), cpx reported by Nishio et al. (2004) (small grey circles) and a host Sviyagin basalt. Also shown are mantle end-members and fields for oceanic basalts (Zindler and Hart, 1986), as well as literature data for peridotite xenoliths (Xu et al., 1998; Yu et al., 2009) and basalts (Kuritani et al., 2011; Xu et al., 2012) from NE China.

Fig. 8. Patterns for PGE and Re in WR xenoliths in this study normalized to primitive upper mantle (Becker et al., 2006). Coherent, continuous depletion from Ir to Re indicates melt extraction and no significant post-melting metasomatism. Low Os/Ir ratios are common in basalt-hosted, off-craton mantle xenoliths (see text for discussion).

Fig. 9. $^{187}Os/^{188}Os$ plotted vs. $^{187}Re/^{188}Os$ (a), Al_2O_3 (b), CaO (c) and MgO (d) for WR

xenoliths in this study (large circles); black lines are linear correlation trends, r^2 are correlation coefficients for the datasets. The equation in the $^{187}Os/^{188}Os$ vs. $^{187}Re/^{188}Os$ diagram (a) shows the slope (implying an 1.9 Ga age) and the initial for the linear regression through all the samples in this study (grey area). Also shown are PUM (Meisel et al., 2001), Sviyagin xenoliths from Guo et al. (2017) (small open circles) and (a-b) peridotite xenoliths from Hannuoba in North China craton (Gao et al., 2002) (crosses); the dotted line in (a) shows the regression for all the Hannuoba xenoliths, which has about the same slope (i.e. defining the same age) as for the Sviyagin suite.

Supplemental Materials

Electronic supplement 1 (ES1): Supplementary figures

Plate 1: Sampling site, basaltic outcrops and xenolith occurrences near Sviyagino.

Plate 2: Photomicrographs of representative Sviyagin spinel peridotite xenoliths.

Plate 3: Major oxides vs. Al_2O_3 vs. for peridotite xenoliths from this study and NE China.

Plate 4. $Mg\#_{WR}$ vs. $Mg\#_{Ol}$ for peridotite xenoliths in this study and from NE China.

Plate 5. MREE-HREE WR patterns for xenoliths in this study and melting modeling.

Plate 6. PM-normalized REE patterns for WR peridotite xenoliths from NE China.

Electronic supplement 2 (ES2): Methods

Electronic supplement 3 (ES3): Analytical results

Table 1: Major elements in whole-rock (WR) samples from XRF analyses.

Table 2: Major elements in minerals by EPMA.

Table 3: Trace elements analyses of WR by LA-ICPMS of fused WR powders.

Table 4: Trace element analyses of pyroxenes by LA-ICPMS.

Table 5: Sr-Nd isotope analyses of clinopyroxenes by TIMS.

Table 6: PGE and Re concentrations and Os isotope analyses of WR xenoliths.

References

Agashev A.M., Ionov D.A, Pokhilenko NP, Golovin AV, Cherepanova Yu.V, Sharygin I.S. (2013)

719 Metasomatism in lithospheric mantle roots: constraints from whole-rock and mineral chemical
720 composition of deformed peridotite xenoliths from kimberlite pipe Udachnaya. Lithos 160-161,
721 201-215.
722 Arai, S., Abe, N. and Ishimaru, S. (2007) Mantle peridotites from the Western Pacific. Gondwana
723 Research 11, 180-199.
724 Bascou J., Doucet L.S., Saumet S., Ionov D.A., Ashchepkov I.V., Golovin A.V. (2011) Seismic
725 velocities, anisotropy and deformation in Siberian cratonic mantle: EBSD data on xenoliths from the
726 Udachnaya kimberlite. Earth Planet. Sci. Lett. 304, 71-84.
727 Becker, H., Horan, M.F., Walker, R.J., Gao, S., Lorand, J.P. and Rudnick, R.L. (2006) Highly
728 siderophile element composition of the Earth's primitive upper mantle: Constraints from new data on
729 peridotite massifs and xenoliths. Geochimica et Cosmochimica Acta 70, 4528-4550.
730 Carlson, R.W. (2005) Application of the Pt–Re–Os isotopic systems to mantle geochemistry and
731 geochronology. Lithos 82, 249-272.
732 Carlson, R.W. and Ionov, D.A. (2019) Compositional characteristics of the MORB mantle and
733 bulk silicate earth based on spinel peridotites from the Tariat Region, Mongolia. Geochimica et
734 Cosmochimica Acta 257, 206-223.
735 Cohen, A.S. and Waters, F.G. (1996) Separation of osmium from geological materials by solvent
736 extraction for analysis by thermal ionisation mass spectrometry, Analytica Chimica Acta, 332,
737 269-275.
738 Deng, L., Liu, Y., Zong, K., Zhu, L., Xu, R., Hu, Z. and Gao, S. (2017) Trace element and Sr
739 isotope records of multi-episode carbonatite metasomatism on the eastern margin of the North China
740 Craton. Geochemistry, Geophysics, Geosystems 18, 220-237.
741 Doucet L.S., Peslier A.H., Ionov D.A., Brandon A.D., Golovin A.V., Goncharov A.G.,
742 Ashchepkov I.V. (2014) High water contents in the Siberian cratonic mantle linked to metasomatism:
743 an FTIR study of Udachnaya peridotite xenoliths. Geochim. Cosmochim. Acta 137, 159-187.
744 Doucet L.S., Ionov D.A., Golovin A.V. (2013) The origin of coarse garnet peridotites in cratonic
745 lithosphere: new data on xenoliths from the Udachnaya kimberlite, central Siberia. Contrib. Miner.
746 Petrol. 165, 1225-1242
747 Gao, S., Rudnick, R.L., Carlson, R.W., McDonough, W.F. and Liu, Y.-S. (2002) Re-Os evidence
748 for replacement of ancient mantle lithosphere beneath the North China craton. Earth Planet Sci Lett
749 198, 307-322.
750 Guo, P., Xu, W.-L., Wang, C.-G., Wang, F., Ge, W.-C., Sorokin, A.A. and Wang, Z.-W. (2017)
751 Age and evolution of the lithospheric mantle beneath the Khanka Massif: Geochemical and Re–Os
752 isotopic evidence from Sviyagino mantle xenoliths. Lithos 282–283, 326-338.
753 Herzberg, C. (2004) Geodynamic information in peridotite petrology. Journal of Petrology 45,
754 2507-2530.
755 Ionov, D. (2002) Mantle structure and rifting processes in the Baikal-Mongolia region:
756 geophysical data and evidence from xenoliths in volcanic rocks. Tectonophysics 351, 41-60.
757 Ionov, D.A. (2007) Compositional variations and heterogeneity in fertile lithospheric mantle:
758 peridotite xenoliths in basalts from Tariat, Mongolia. Contrib. Mineral. Petrol. 154, 455-477.
759 Ionov, D.A. (2010) Petrology of mantle wedge lithosphere: New data on supra-subduction zone
760 peridotite xenoliths from the andesitic Avacha volcano, Kamchatka. Journal of Petrology 51,
761 327-361.
762 Ionov, D.A., Ashchepkov, I. and Jagoutz, E. (2005). The provenance of fertile off-craton

lithospheric mantle: Sr-Nd isotope and chemical composition of garnet and spinel peridotite xenoliths from Vitim, Siberia. Chemical Geology 217, 41-75.

Ionov, D.A., Bigot, F. and Braga, R. (2017) The Provenance of the Lithospheric Mantle in Continental Collision Zones: Petrology and Geochemistry of Peridotites in the Ulten–Nonsberg Zone (Eastern Alps). Journal of Petrology 58, 1451-1472.

Ionov, D.A., Chanefo, I. and Bodinier, J.-L. (2005) Origin of Fe-rich lherzolites and wehrlites from Tok, SE Siberia by reactive melt percolation in refractory mantle peridotites. Contributions to Mineralogy and Petrology 150, 335-353.

Ionov, D.A., Chazot, G., Chauvel, C., Merlet, C. and Bodinier, J.-L. (2006a) Trace element distribution in peridotite xenoliths from Tok, SE Siberian craton: A record of pervasive, multi-stage metasomatism in shallow refractory mantle. Geochimica et Cosmochimica Acta 70, 1231-1260.

Ionov, D.A., Doucet, L.S., Carlson, R.W., Golovin, A.V. and Korsakov, A.V. (2015) Post-Archean formation of the lithospheric mantle in the central Siberian craton: Re–Os and PGE study of peridotite xenoliths from the Udachnaya kimberlite. Geochimica et Cosmochimica Acta 165, 466-483.

Ionov DA, Doucet LS, Pogge von Strandmann PAE, Golovin AV, Korsakov AV (2017) Links between deformation, chemical enrichments and Li-isotope compositions in the lithospheric mantle of the central Siberian craton. Chem. Geol. 475, 105-121,

Ionov, D.A., Grégoire, M. and Prikhod'ko, V.S. (1999) Feldspar-Ti-oxide metasomatism in off-cratonic continental and oceanic upper mantle. Earth and Planetary Science Letters 165, 37-44.

Ionov, D.A. and Hofmann, A.W. (2007) Depth of formation of sub-continental off-craton peridotites. Earth and Planetary Science Letters 261, 620-634.

Ionov, D.A., Hofmann, A.W., Merlet, C., Gurenko, A.A., Hellebrand, E., Montagnac, G., Gillet, P. and Prikhodko, V.S. (2006b) Discovery of whitlockite in mantle xenoliths: Inferences for water- and halogen-poor fluids and trace element residence in the terrestrial upper mantle. Earth and Planetary Science Letters 244, 201-217.

Ionov, D.A., Prikhodko, V.S. and O'Reilly, S.Y. (1995) Peridotite xenoliths in alkali basalts from the Sikhote-Alin, southeastern Siberia, Russia: trace element signatures of mantle beneath a convergent continental margin. Chem Geol 120, 275-294.

Ionov, D.A., Shirey, S.B., Weis, D. and Brügmann, G. (2006c) Os-Hf-Sr-Nd isotope and PGE systematics of spinel peridotite xenoliths from Tok, SE Siberian craton: Effects of pervasive metasomatism in shallow refractory mantle. Earth and Planetary Science Letters 241, 47-64.

Kalfoun, F., Ionov, D. and Merlet, C. (2002) HFSE residence and Nb-Ta ratios in metasomatised, rutile-bearing mantle peridotites. Earth and Planetary Science Letters 199, 49-65.

Kuritani, T., Ohtani, E. and Kimura, J.-I. (2011) Intensive hydration of the mantle transition zone beneath China caused by ancient slab stagnation. Nature Geosci 4, 713-716.

Liu, J., Cai, R., Pearson, D.G., Scott, J.M., 2019. Thinning and destruction of the lithospheric mantle root beneath the North China Craton: A review. Earth-Science Reviews 196, 102873.

Liu, J., Rudnick, R.L., Walker, R.J., Gao, S., Wu, F.-y., Piccoli, P.M., Yuan, H., Xu, W.-l. and Xu, Y.-G. (2011) Mapping lithospheric boundaries using Os isotopes of mantle xenoliths: An example from the North China Craton. Geochimica et Cosmochimica Acta 75, 3881-3902.

Liu, K., Zhang, J., Wilde, S.A., Liu, S., Guo, F., Kasatkin, S.A., Golozoubov, V.V., Ge, M., Wang, M. and Wang, J. (2017a) U-Pb dating and Lu-Hf isotopes of detrital zircons from the southern Sikhote-Alin orogenic belt, Russian Far East: Tectonic implications for the Early Cretaceous

807 evolution of the Northwest Pacific margin. Tectonics 36, 2555–2598.
808 Liu, Y., Li, W., Feng, Z., Wen, Q., Neubauer, F. and Liang, C. (2017b) A review of the Paleozoic
809 tectonics in the eastern part of Central Asian Orogenic Belt. Gondwana Research 43, 123-148.
810 Lorand, J.-P. and Grégoire, M. (2006) Petrogenesis of base metal sulphide assemblages of some
811 peridotites from the Kaapvaal craton (South Africa). Contrib. Mineral. Petrol. 151, 521-538.
812 Luguet, A. and Reisberg, L. (2016) Highly Siderophile Element and ^{187}Os Signatures in
813 Non-cratonic Basalt-hosted Peridotite Xenoliths: Unravelling the Origin and Evolution of the
814 Post-Archean Lithospheric Mantle. Reviews in Mineralogy & Geochemistry 81, 305-368.
815 McDonough, W.F. and Sun, S.-s. (1995) The composition of the Earth. Chem Geol 120, 223-253.
816 Meisel, T., Walker, R.J., Irving, A.J. and Lorand, J.-P. (2001) Osmium isotopic compositions of
817 mantle xenoliths: a global perspective. Geochim. Cosmochim. Acta 65, 1311-1323.
818 Menzies, M.A., Fan, W. and Zhang, M. (1993) Paleozoic and Cenozoic lithoprobes and the loss
819 of >120 km of Archaean lithosphere, Sino-Korean craton. Geol. Soc. London Spec. Publ. 76, 71-81.
820 Nishio, Y., Nakai, S., Yamamoto, J., Sumino, H., Matsumoto, T., Prikhod'ko, V.S. and Arai, S.
821 (2004) Lithium isotopic systematics of the mantle-derived ultramafic xenoliths: implications for
822 EM1 origin. Earth Planet Sci Lett 217, 245-261.
823 Okamura, S., Arculus, R.J. and Martynov, Y.A. (2005) Cenozoic Magmatism of the North-Eastern
824 Eurasian Margin: The Role of Lithosphere Versus Asthenosphere. J. Petrol. 46, 221-253.
825 Okamura, S., Martynov, Y.A., Furuyama, K. and Nagao, K. (1998) K-Ar ages of the basaltic
826 rocks from far east Russia: Constraints on the tectono-magmatism associated with the Japan Sea
827 opening. The Island Arc 7, 271-282.
828 Pearson, D.G., Canil, D. and Shirey, S.B. (2014) Mantle samples included in volcanic rocks:
829 Xenoliths and diamonds, in: Carlson, R.W. (Ed.), Treatise on Geochemistry (Second Edition).
830 Elsevier, Oxford, pp. 169-253.
831 Pearson, D.G., Irvine, G.J., Ionov, D.A., Boyd, F.R. and Dreibus, G.E. (2004) Re-Os isotope
832 systematics and platinum group element fractionation during mantle melt extraction: a study of
833 massif and xenolith peridotite suites. Chem Geol 208, 29-59.
834 Pearson, D.G. and Wittig, N. (2014) The Formation and Evolution of Cratonic Mantle
835 Lithosphere – Evidence from Mantle Xenoliths, Treatise on Geochemistry (Second Edition). Elsevier,
836 Oxford, pp. 255-292.
837 Reisberg, L. and Lorand, J.P. (1995) Longevity of sub-continental mantle lithosphere from
838 osmium isotope systematics in orogenic peridotite massifs. Nature 376, 159-162.
839 286-308.
840 Reisberg, L., Zhi, X., Lorand, J.-P., Wagner, C., Peng, Z. and Zimmermann, C. (2005). Re–Os and
841 S systematics of spinel peridotite xenoliths from east central China: Evidence for contrasting effects
842 of melt percolation. Earth Planet Sci Lett 239, 286-308.
843 Rudnick, R.L., Gao, S., Ling, W.-l., Liu, Y.-s. and McDonough, W.F. (2004) Petrology and
844 geochemistry of spinel peridotite xenoliths from Hannuoba and Qixia, North China craton. Lithos 77,
845 609-637.
846 Rudnick, R.L. and Walker, R.J. (2009) Interpreting ages from Re–Os isotopes in peridotites
847 Lithos 112, Supplement 2, 1083-1095.
848 Takazawa, E., Frey, F.A., Shimizu, N. and Obata, M. (2000) Whole rock compositional variations
849 in an upper mantle peridotite (Horoman, Hokkaido, Japan): Are they consistent with a partial melting
850 process. Geochimica et Cosmochimica Acta 64, 695-716.

Walker, R.J. (2016) Siderophile Elements in Tracing Planetary Formation and Evolution. Geochemical Perspectives 5, 1-145.

Walker, R.J., Carlson, R.W., Shirey, S.B. and Boyd, F.R. (1989) Os, Sr, Nd, and Pb isotope systematics of southern African peridotite xenoliths: Implications for the chemical evolution of subcontinental mantle. Geochim. Cosmochim. Acta 53, 1583-1595.

Wang, K.-L., Prikhodko, V., O'Reilly, S.Y., Griffin, W.L., Pearson, N.J., Kovach, V., Iizuka, Y. and Chien, Y.-H. (2015) Ancient mantle lithosphere beneath the Khanka massif in the Russian Far East: in situ Re-Os evidence. Terra Nova 27, 277-284.

Wilde, S.A. (2015) Final amalgamation of the Central Asian Orogenic Belt in NE China: Paleo-Asian Ocean closure versus Paleo-Pacific plate subduction — A review of the evidence. Tectonophysics 662, 345-362.

Wu, F.-y., Walker, R.J., Ren, X.-w., Sun, D.-y. and Zhou, X.-h. (2003) Osmium isotopic constraints on the age of lithospheric mantle beneath northeastern China. Chem Geol 196, 107-129.

Wu, F.-Y., Walker, R.J., Yang, Y.-H., Yuan, H.-L. and Yang, J.-H. (2006) The chemical-temporal evolution of lithospheric mantle underlying the North China Craton. Geochimica et Cosmochimica Acta 70, 5013-5034.

Xu, B., Zhao, P., Wang, Y., Liao, W., Luo, Z., Bao, Q. and Zhou, Y. (2015) The pre-Devonian tectonic framework of Xing'an–Mongolia orogenic belt (XMOB) in north China. Journal of Asian Earth Sciences 97, 183-196.

Xu, Y., Menzies, M.A., Vroon, P., Mercier, J.-C. and Lin, C. (1998) Texture-temperature-geochemistry relationships in the upper mantle as revealed from spinel peridotite xenoliths from Wangqing, NE China. J. Petrol. 39, 469-493.

Xu, Y.-G. (2014) Recycled oceanic crust in the source of 90–40Ma basalts in North and Northeast China: Evidence, provenance and significance. Geochimica et Cosmochimica Acta 143, 49-67.

Xu, Y.-G., Menzies, M.A., Thirlwall, M.F., Huang, X.-L., Liu, Y. and Chen, X.-M. (2003) "Reactive" harzburgites from Huinan, NE China: products of the lithosphere-asthenosphere interaction during lithospheric thinning? Geochim. Cosmochim. Acta 67, 487-505.

Xu, Y.-G., Zhang, H.-H., Qiu, H.-N., Ge, W.-C. and Wu, F.-Y. (2012) Oceanic crust components in continental basalts from Shuangliao, Northeast China: Derived from the mantle transition zone? Chem Geol 328, 168-184.

Xu, Y.G., Mercier, J.-C.C., Menzies, M.A., Ross, J.V., Harte, B., Lin, C. and Shi, L. (1996) K-rich glass-bearing wehrlite xenoliths from Yitong, northeastern China: petrological and chemical evidence for mantle metasomatism. Contrib. Mineral. Petrol. 125, 406-420.

Yu, S.-Y., Xu, Y.-G., Huang, X.-L., Ma, J.-L., Ge, W.-C., Zhang, H.-H. and Qin, X.-F. (2009) Hf-Nd isotopic decoupling in continental mantle lithosphere beneath Northeast China: Effects of pervasive mantle metasomatism. Journal of Asian Earth Sciences 35, 554-570.

Zhang, Y.-L., Liu, C.-Z., Ge, W.-C., Wu, F.-Y. and Chu, Z.-Y. (2011) Ancient sub-continental lithospheric mantle (SCLM) beneath the eastern part of the Central Asian Orogenic Belt (CAOB): Implications for crust-mantle decoupling. Lithos 126, 233-247.

Zhang, Y.-L., Ge, W.C., Sun, J., Yang, H., Liu, Z.C., Liu, J.G., 2019. Age and composition of the subcontinental lithospheric mantle beneath the Xing'an-Mongolia Orogenic Belt: Implications for the construction of microcontinents during accretionary orogenesis. Lithos 326, 556-571.

Zhao, P., Jahn, B.-m. and Xu, B. (2017) Elemental and Sr-Nd isotopic geochemistry of Cretaceous to Early Paleogene granites and volcanic rocks in the Sikhote-Alin Orogenic Belt

(Russian Far East): implications for the regional tectonic evolution. Journal of Asian Earth Sciences 146, 383-401.

Zhou, J.-B., Wilde, S.A., Zhao, G.-C. and Han, J. (2018) Nature and assembly of microcontinental blocks within the Paleo-Asian Ocean. Earth-Science Reviews 186, 76-93.

Zhu, R.-X., Yang, J.-H. and Wu, F.-Y. (2012) Timing of destruction of the North China Craton. Lithos 149, 51-60.

Zindler, A. and Hart, S. (1986) Chemical geodynamics. Ann. Rev. Earth Planet. Sci. 14, 493-571.

Zou, D., Liu, Y., Hu, Z., Gao, S., Zong, K., Xu, R., Deng, L., He, D. and Gao, C. (2014) Pyroxenite and peridotite xenoliths from Hexigten, Inner Mongolia: Insights into the Paleo-Asian Ocean subduction-related melt/fluid–peridotite interaction. Geochimica et Cosmochimica Acta 140, 435-454.

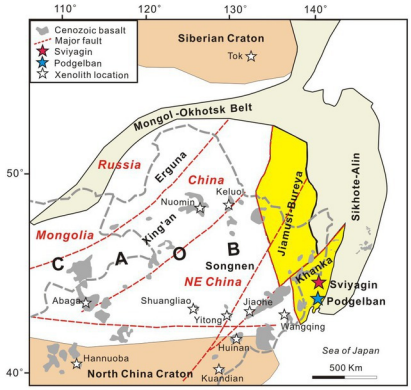
110°
120°
130°
140°
50°
40°
Cenozoic basalt
Major fault
Sviyagin
Podgelban
Xenolith location
Siberian Craton
Tok
Mongol -Okhotsk Belt
Russia
Erguna
China
Keluo
Nuomin
Xing an
Mongolia
C
A
O
B
Songnen
NE China
Jiamusi-Bureya
Khanka
Sikhote-Alin
Sviyagin
Podgelban
Abaga
Shuangliao
Jiaohe
Yitong
Wangqing
Hunan
Hannuoba
North China Craton
Kuandian
Sea of Japan
500 Km

Fig.1

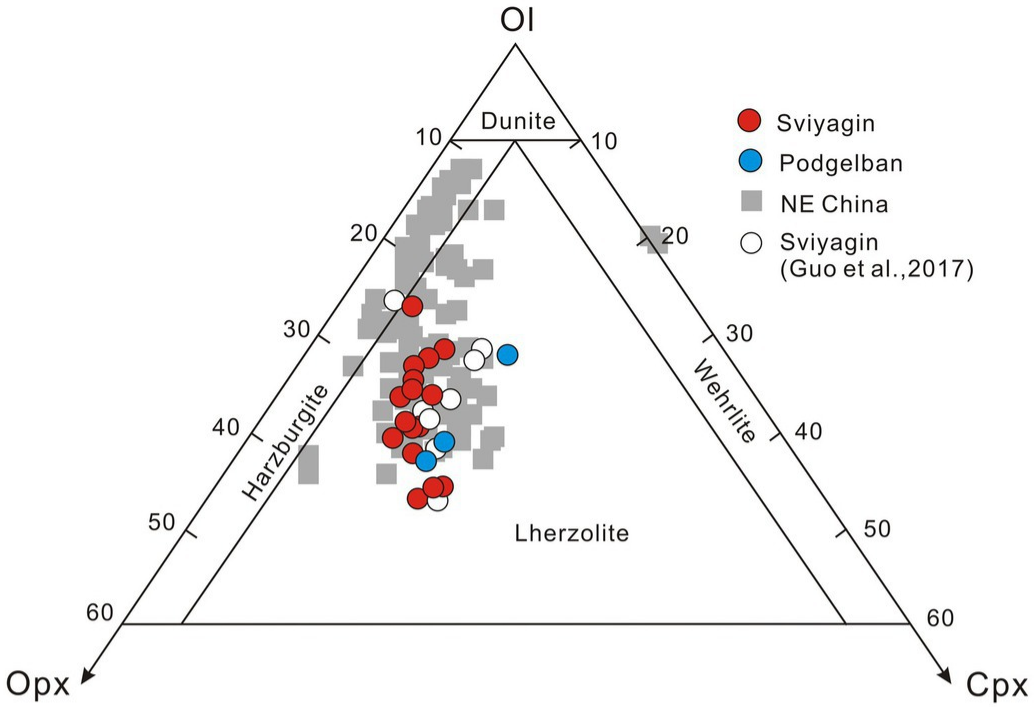
Ol
Dunite
10
10
20
20
30
30
40
40
50
50
60
60
Harzburgite
Wehrlite
Lherzolite
Opx
Cpx
Sviyagin
Podgelban
NE China
Sviyagin
(Guo et al.,2017)

Fig.2

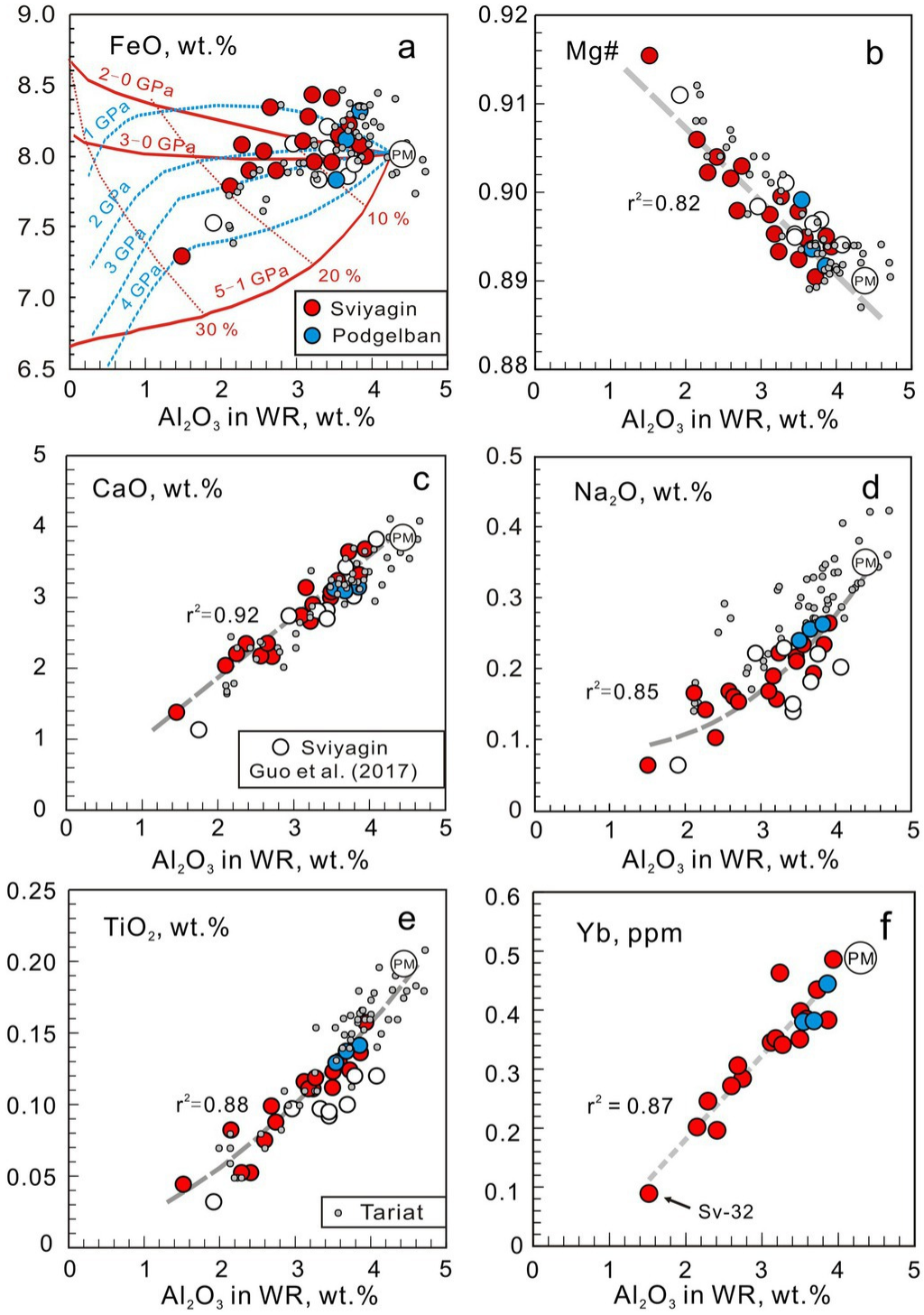
FeO, wt.%
a
2–0 GPa
1 GPa
3–0 GPa
2 GPa
3 GPa
4 GPa
5–1 GPa
10 %
20 %
30 %
PM
Sviyagin
Podgelban
Al2O3 in WR, wt.%
Mg#
b
r2=0.82
CaO, wt.%
c
r2=0.92
Sviyagin
Guo et al. (2017)
Na2O, wt.%
d
r2=0.85
TiO2, wt.%
e
r2=0.88
Tariat
Yb, ppm
f
r2 = 0.87
Sv-32

Fig.3

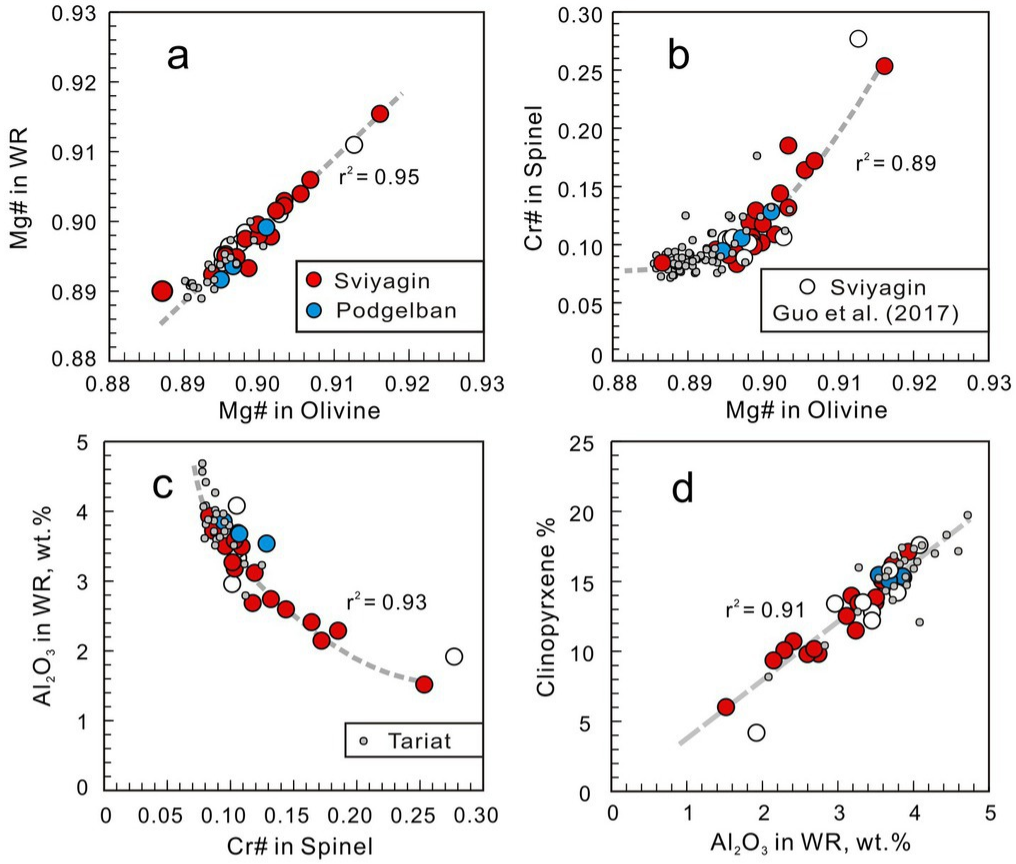
a
Mg# in WR
Mg# in Olivine
r² = 0.95
Sviyagin
Podgelban
b
Cr# in Spinel
Mg# in Olivine
r² = 0.89
Sviyagin
Guo et al. (2017)
c
Al2O3 in WR, wt.%
Cr# in Spinel
r² = 0.93
Tariat
d
Clinopyrxene %
Al2O3 in WR, wt.%
r² = 0.91

Fig.4

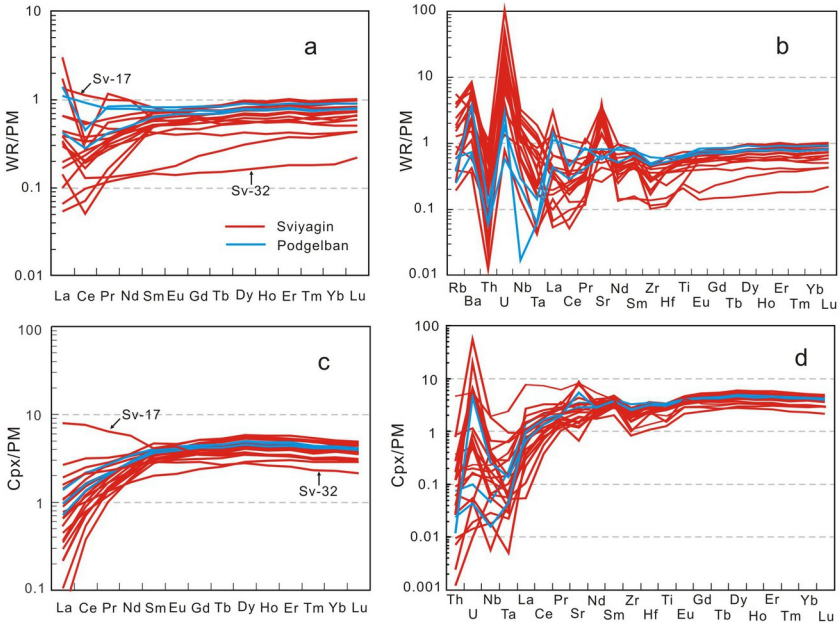
a
WR/PM
Sv-17
Sv-32
Sviyagin
Podgelban
La Ce Pr Nd Sm Eu Gd Tb Dy Ho Er Tm Yb Lu
b
WR/PM
Rb Ba Th U Nb Ta La Ce Pr Sr Nd Sm Zr Hf Ti Eu Gd Tb Dy Ho Er Tm Yb Lu
c
Cpx/PM
Sv-17
Sv-32
La Ce Pr Nd Sm Eu Gd Tb Dy Ho Er Tm Yb Lu
d
Cpx/PM
Th U Nb Ta La Ce Pr Sr Nd Sm Zr Hf Ti Eu Gd Tb Dy Ho Er Tm Yb Lu

Fig. 5

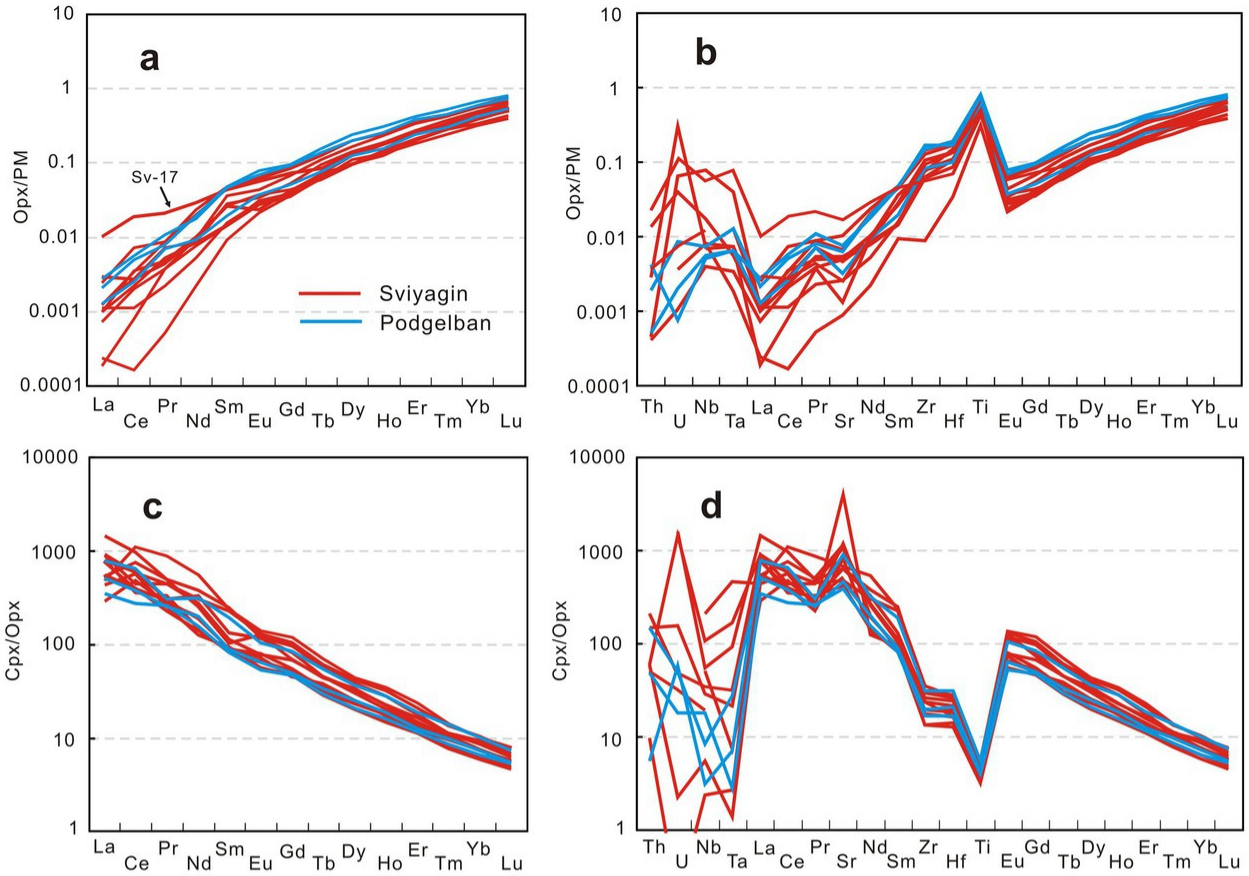
a
b
c
d
Opx/PM
Cpx/Opx
Sv-17
Sviyagin
Podgelban
10
1
0.1
0.01
0.001
0.0001
10000
1000
100
10
1
La Ce Pr Nd Sm Eu Gd Tb Dy Ho Er Tm Yb Lu
Th U Nb Ta La Ce Pr Sr Nd Sm Zr Hf Ti Eu Gd Tb Dy Ho Er Tm Yb Lu

Fig.6

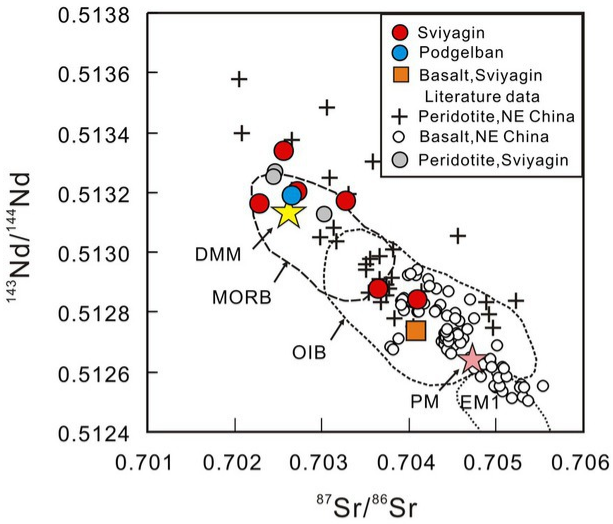
Sviyagin
Podgelban
Basalt,Sviyagin
Literature data
Peridotite,NE China
Basalt,NE China
Peridotite,Sviyagin
DMM
MORB
OIB
PM
EM1
0.5138
0.5136
0.5134
0.5132
0.5130
0.5128
0.5126
0.5124
0.701
0.702
0.703
0.704
0.705
0.706
143Nd/144Nd
87Sr/86Sr

Fig.7

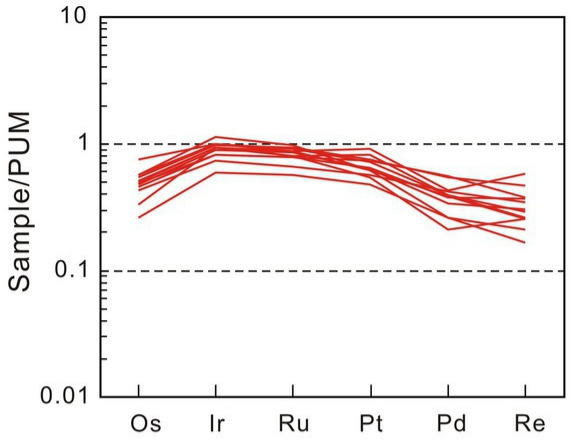

Fig.8

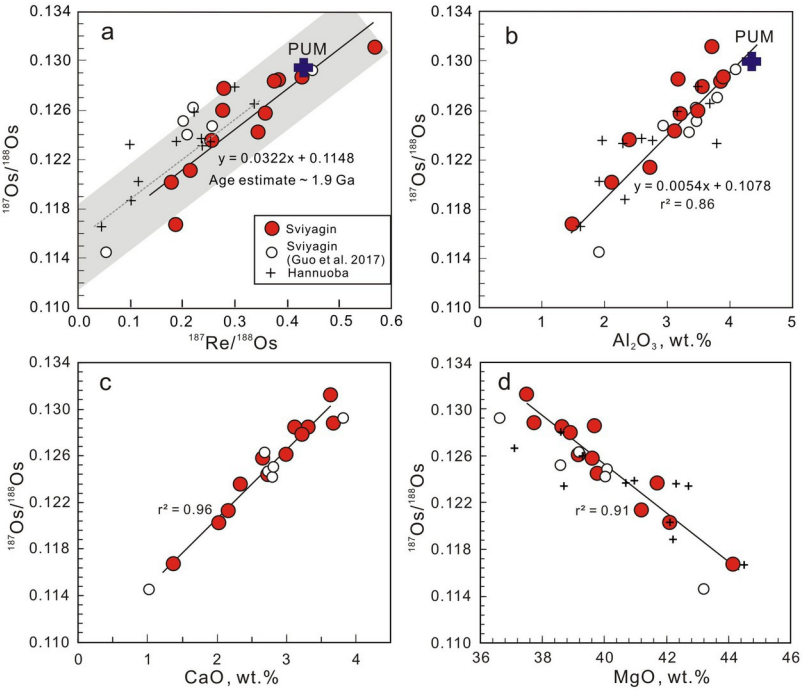
a
PUM
y = 0.0322x + 0.1148
Age estimate ~ 1.9 Ga
Sviyagin
Sviyagin (Guo et al. 2017)
Hannuoba
$^{187}Os/^{188}Os$
$^{187}Re/^{188}Os$
b
PUM
y = 0.0054x + 0.1078
r² = 0.86
Al_2O_3, wt.%
c
r² = 0.96
CaO, wt.%
d
r² = 0.91
MgO, wt.%

Fig. 9

Table 1

Summary of data for peridotite xenoliths from far eastern Russia

Sample	Al_2O_3	CaO	Mg#	Mg#	Cr#	T	Calculated modal abundance				Sr-Nd	Re-Os
no.	WR, wt.%		WR	ol	spl	°C	ol	opx	cpx	sp		
Sviyagin (spinel lherzolites)												
Sv-4	2.74	2.17	0.903	0.903	0.13	933	61.8	26.9	9.8	1.6	+	+
Sv-7	2.41	2.35	0.904	0.906	0.16	953	66.4	21.1	10.7	1.7	+	+
Sv-8	n.d.	n.d.	n.d.	0.899	0.13	925	n.d.	n.d.	n.d.	n.d.	+	
Sv-9	3.93	3.68	0.894	0.896	0.08	892	52.4	28.2	17.1	2.4	+	+
Sv-13	3.24	2.66	0.893	0.899	0.10	845	57.0	28.7	11.5	2.1		+
Sv-14	2.29	2.21	0.902	0.903	0.19	898	65.8	23.0	10.1	1.4		
Sv-15	3.50	3.00	0.898	0.902	0.11	877	55.7	28.1	13.5	2.2		+
Sv-16	3.50	3.08	0.892	0.894	0.10	810	57.6	25.6	13.9	2.5		
Sv-17	2.60	2.17	0.902	0.902	0.14	995	63.0	25.2	9.8	1.3	+	
Sv-18	3.12	2.74	0.897	0.898	0.12	972	58.9	27.3	12.5	1.3		+
Sv-20	2.15	2.04	0.906	0.907	0.17	914	65.0	24.1	9.4	1.0		+
Sv-22	3.18	3.14	0.895	0.896	0.10	933	59.5	24.4	14.0	1.9		+
Sv-24	3.58	3.24	0.895	0.897	0.10	1000	56.2	26.4	15.1	2.0		+
Sv-27	2.68	2.35	0.898	0.900	0.12	816	62.9	24.8	10.2	1.7		
Sv-28	3.27	2.90	0.900	0.900	0.10	952	59.7	24.4	13.5	2.0		
Sv-29	3.86	3.32	0.895	0.895	0.09	970	55.9	25.9	15.3	2.5		+
Sv-32	1.52	1.38	0.915	0.916	0.25	988	72.0	21.5	6.0	0.9	+	+
8701-4	3.72	3.64	0.890	0.887	0.09	922	51.3	30.5	16.2	2.4		+
Podgelban (spinel lherzolites)												
Pod-1	3.54	3.13	0.899	0.901	0.13	993	65.7	16.5	15.5	3.2	+	
Pod-3	3.86	3.15	0.892	0.894	0.09	1054	57.2	25.7	15.4	2.5		
Pod-4	3.68	3.09	0.894	0.897	0.11	1033	55.1	28.5	15.1	2.2		

Samples Sv-9 and Sv-14 have porphyroblastic microstructure, all other samples are protogranular.

Sample Sv-8 was not analyzed for whole-rock composition.

Mg#, $Mg/(Mg+Fe)_{at}$; Cr#, $Cr/(Al+Cr)_{at}$; ol, olivine; opx, orthopyroxene; cpx, clinopyroxene; sp, spinel.

Equilibration temperatures (T) estimated using cpx-opx thermometry with a fixed P = 1.5 GPa (ES2).

Modal estimates obtained by least-squares method from whole-rock (WR) and mineral analyses (ES2).

n.d., not determined. (+) Samples with Sm-Nd and/or Re-Os isotope data

Table 2

Abundances of HSE, $^{187}Re/^{188}Os$ and $^{187}Os/^{188}Os$ ratios and model age estimates for peridotites in this study

Sample	Os	Ir	Ru	Pt	Pd	Re	$^{187}Re/^{188}Os$	$^{187}Os/^{188}Os$	2SE	T_{MA}	T_{RD}
	ppb	ppb	ppb	ppb	ppb	ppb				Ga	Ga
Sv-4	2.187	3.48	6.12	4.67	2.68	0.088	0.217	0.12128	0.00006	2.25	1.14
Sv-7	1.955	3.20	5.59	6.10	2.78	0.090	0.257	0.12358	0.00007	2.00	0.82
Sv-9	2.107	3.35	6.46	5.69	3.84	0.162	0.433	0.12876	0.00007	19.10	0.12
Sv-13	1.784	2.83	5.46	4.88	2.63	0.128	0.361	0.12573	0.00008	3.06	0.53
Sv-15	1.832	3.11	5.98	4.74	2.36	0.104	0.279	0.12608	0.00007	1.34	0.48
Sv-18	1.277	3.22	5.54	4.09	1.47	0.089	0.348	0.12437	0.00008	3.51	0.72
Sv-20	2.902	3.45	6.35	5.43	2.76	0.100	0.182	0.12021	0.00005	2.18	1.28
Sv-22	1.883	2.84	5.45	5.51	3.87	0.130	0.385	0.12846	0.00006	1.35	0.16
Sv-24	1.001	2.06	3.89	3.61	1.82	0.058	0.284	0.12788	0.00007	0.68	0.24
Sv-29	1.663	2.55	4.56	4.32	2.97	0.120	0.380	0.12843	0.00006	1.25	0.16
Sv-32	2.179	3.90	6.77	4.62	1.83	0.073	0.192	0.11669	0.00009	3.10	1.75
8701-4	1.925	3.25	6.02	6.83	2.99	0.199	0.570	0.13122	0.00016	0.72	-0.22

SE, standard error. MA, model age; RD, rhenium-depletion age.

T_{RD} and T_{MA} are calculated relative to the primitive upper mantle : $^{187}Re/^{188}Os$= 0.4353; $^{187}Os/^{188}Os$= 0.1296; $\lambda = 1.6660E{-}11$

Median T_{MA} value for all the samples is 2.1 Ga; average T_{MA} value (excepting the anomalously high value for Sv-9) is 1.95 Ga.